Time and space resolved operando synchrotron X-ray and Neutron diffraction study of NMC811/Si-Gr 5 Ah pouch cells

Graae, Kristoffer Visti; Li, Xinyu; Sørensen, Daniel Risskov; Ayerbe, Elixabete; Boyano, Iker; Sheptyakov, Denis; Jørgensen, Mads Ry Vogel; Norby, Poul

Published in:
Journal of Power Sources

Link to article, DOI:
10.1016/j.jpowsour.2023.232993

Publication date:
2023

Document Version
Publisher's PDF, also known as Version of record

Journal of Power Sources 570 (2023) 232993

Contents lists available at ScienceDirect

Journal of Power Sources

journal homepage: www.elsevier.com/locate/jpowsour

Time and space resolved operando synchrotron X-ray and Neutron diffraction study of NMC811/Si–Gr 5 Ah pouch cells

Kristoffer Visti Graae [a,*], Xinyu Li [a], Daniel Risskov Sørensen [b,c], Elixabete Ayerbe [d], Iker Boyano [d], Denis Sheptyakov [e], Mads Ry Vogel Jørgensen [b,c], Poul Norby [a]

[a] Department of Energy Conversion and Storage, Technical University of Denmark, Fysikvej 310, Kongens Lyngby, 2800, Denmark
[b] Department of Chemistry & iNANO, University of Aarhus, Aarhus C, 8000, Denmark
[c] MAX IV Laboratory, Lund University, Lund, SE-221 00, Sweden
[d] CIDETEC, Basque Research and Technology Alliance (BRTA), Paseo Miramón 196, Donostia-San Sebastián, 5 20014, Spain
[e] Laboratory for Neutron Scattering and Imaging, Paul Scherrer Institut, Villigen PSI, 5232, Switzerland

HIGHLIGHTS

- 2D diffraction mapping of lateral inhomogeneities in Si–Gr 5 Ah Pouch cells.
- Correlation between volume expansion and lateral inhomogeneities.
- Disconnected charge/discharge patterns of Si and graphite components were found.
- Difference in cathode and anode lithium inhomogeneities.

GRAPHICAL ABSTRACT

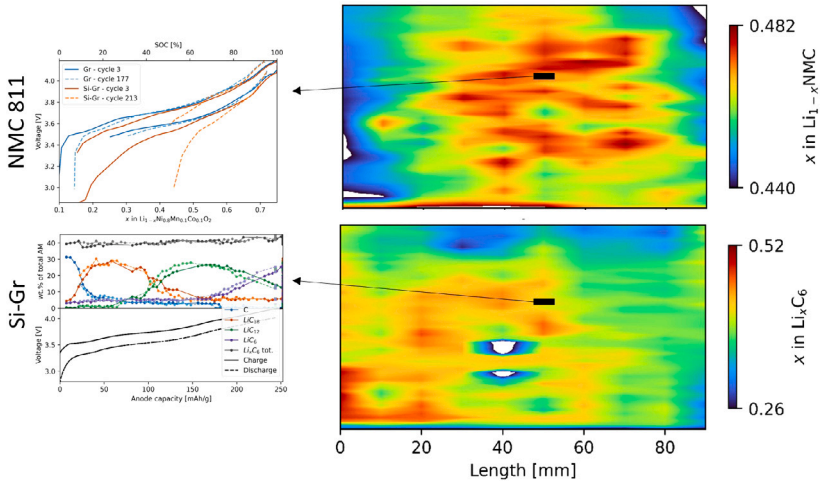

ARTICLE INFO

Keywords:
Silicon–graphite
In situ
Pouch cell
NMC 811
Neutron diffraction
XRD

ABSTRACT

Silicon–Graphite blended electrodes in Li-ion batteries have been proposed as a way to harness the high capacity of Si as an anode material, while minimising the negative effects of their large volume expansion. NMC 811 is the current state-of-the-art layered oxide cathode material, where the cobalt content of the cathode has been minimised. These are the two of the most promising materials for achieving electric vehicle targets in terms of performance, cyclability and price, however their degradation mechanism is not fully understood. Here these two materials have been used to manufacture 5 Ah prototype multi-layer pouch cells, which are aged and then studied using two complimentary diffraction techniques. Neutron diffraction has enabled a quantitative analysis of phase transitions in Si–Gr anodes in a pristine and degraded cell, and the alloying behaviour of Si and Li has been inferred by comparison of identical cells with either graphite or Si–Gr anodes. Synchrotron X-ray Diffraction has been used to make an operando 2D map of the cathode and anode lithiation in the pouch cell, as well as to map the volume expansion across the cell. This approach has revealed that

* Corresponding author.
E-mail addresses: kvisgr@dtu.dk (K.V. Graae), lixiu@dtu.dk (X. Li), daniel.sorensen@morrowbatteries.com (D.R. Sørensen), eayerbe@cidetec.es (E. Ayerbe), iboyano@cidetec.es (I. Boyano), denis.cheptiakov@psi.ch (D. Sheptyakov), mads@chem.au.dk (M.R.V. Jørgensen), pnor@dtu.dk (P. Norby).

https://doi.org/10.1016/j.jpowsour.2023.232993
Received 11 November 2022; Received in revised form 17 March 2023; Accepted 22 March 2023
Available online 13 April 2023

degradation entails significant inhomogeneities across both electrodes, linked to the inhomogeneous volume expansion of the Si–Gr anodes.

1. Introduction

Advanced Li-ion batteries will still play an important role in future energy systems. Improving performance by reducing degradation is a complex process, requiring a holistic approach to the complex processes that contribute to the deterioration of a cell's capacity over hundreds or thousands of cycles. Transport accounts for a fifth of global CO_2 emissions, 45.1% of which comes from passenger vehicles [1]. Transitioning to electrically powered vehicles is therefore a central part of a green transition. To that end it will be crucial to reduce the cost of batteries, enhance cyclability, as well as increasing their gravimetric and volumetric capacity.

Li(Ni,Mn,Co,)O_2 (NMC) is one of the most widely used cathode materials in batteries powering electric vehicles. This large scale adoption will however signify a dramatic increase in mining for cobalt, with the battery industry already accounting for two thirds of global demand. Cobalt is not only the most expensive element of NMC batteries, but is largely extracted under problematic conditions, undermining the sustainable credentials of a shift to a battery-powered economy. Limiting the amount of cobalt used in NMC is thus highly desirable, with NMC 811 ($LiNi_{0.8}Mn_{0.1}Co_{0.1}O_2$) being the current state of the art material in the battery field [2].

On the anode side of the battery, graphite is widely used across most Li-ion battery technologies. The use of silicon anodes has long been proposed as an alternative, due to its very high theoretical capacity, with each Si atom being able to bind 4 Li atoms, thus having a theoretical gravimetric capacity of 3579 mAh/g in the case of $Li_{15}Si_4$ at room temperature, compared to graphite, which can store one Li atom for every six C atoms, with a resulting gravimetric capacity of 370 mAh/g [3–6]. Si anodes have the significant disadvantage of a rapid decline in stability during prolonged cycling, due to large volume fluctuation during charge and discharge, slow ion diffusion and low conductivity. This leads to particles breaking down and loss of electrical contact [7–9].

Approaches to using the advantages of Si anodes while limiting their drawbacks include nanoengineering in the form of coatings on Si particles, development of cycling protocols within narrower potential and capacity limits, binder formulations permitting volume expansion, and finally blended electrodes [9–11]. Graphite's wide use in the battery industry due to its low surface area, high conductivity, electrochemical stability, low tap-density and chemical/physical stability makes it suitable for designing an electrode in combination with Si [4–6]. There have been different approaches to Si–Gr anodes, in terms of combining them with specific binder and electrolyte formulations to increase stability [12,13], nanoengineering including coating Si particles with graphite [6,7], and simply tweaking the ratio of Si to graphite, which has a significant influence on the electrochemical and mechanical behaviour of the anode. At the high end a ratio of 20% can result in a continuous graphite structure serving as backbone, with relatively high stability and low electrolyte decomposition compared to Si anodes, while still being enough to triple the gravimetric capacity compared to a graphite electrode [14]. Current commercial Si–Gr electrodes have Si contents in the range of 2–3 wt.% [15,16], but contents of at least 5–7 wt% are probably needed to get worthwhile performance gains [17,18].

Si–Gr anodes have obtained good performances in half cells, while performance in full cells is still lacking, due to limited Li^+ availability. The loss of cyclable Li to the SEI layer during initial cycles with low coulombic efficiency is irrelevant in half cells with an infinite supply of Li, but is critical for performance in full cells. High-performing cells with Si–Gr anodes necessitate a thorough understanding of the effect of cross talk between electrodes, and between Si and Gr particles in the anode. The mechanical effect of the large volume expansion of Si particles on the electrode cohesiveness, as well as on the capacity suppression of graphite is also important [18].

Understanding the mechanisms of (de)lithiation in Si–Gr anodes as well as degradation mechanisms is essential to improving the cycle life and thus the viability of Si–Gr anodes in combination with state-of-the-art cathodes. Heubner et al. elucidate the electrochemical behaviour of Si and Gr relative to each other using a cell with separate Si and Gr anodes, short-circuited to provide the same thermodynamics of blended electrodes, but allowing them to independently monitor the activity of Si and Gr [8]. To study the effect of Li^+ cross-talk between Gr and Si in actual full cells, a direct method of studying the same effect in actual electrodes is necessary. Pietsch et al. use X-ray tomography to confirm that in graphite electrodes as well as in Si–Gr electrodes expansion is highly anisotropic, with electrodes expanding 25 times more perpendicular to the current collector than parallel to it, meaning that the electrode structure or the cell housing lead to a highly anisotropic volume expansion [14]. Other groups have also extensively used dilatometry and pressure measurements to track the volume expansion and its effect on cell performance [3,19,20], notably Vidal et al. who combine it with X-ray Computed Micro tomography (XCMT) in pouch cells and 18650 cells [21]. Moon et al. use a combination of XRD, electron microscopy techniques and dilatometry to describe the relative behaviour of Si and Gr in full cells, and give insights into the effect the mechanical changes undergone in the electrodes has on the graphite component of the blended electrodes [18]. Neutrons can be a very powerful tool in characterising anodes in real time, but have not until now been used extensively. Most recently Richter et al. have investigated full cells with Si–Gr cells using operando neutron diffraction. They study 18650 cells during charge, tracking LiC_6 and LiC_{12} phase fractions. They use the intensity change of a LiC_6 (001) peak and a LiC_{12} (002) peak to track the lithiation of graphite, and from that infer the behaviour of Si at low temperatures [22].

An effect that has not been fully investigated is the effect spatial inhomogeneities in large-format cells has on the degradation of Si–Gr anodes. The negative effects of heterogeneities in lithiation across electrodes and within cells has been documented extensively in other Li-ion chemistries using X-ray diffraction and neutron diffraction. Inhomogeneities across pouch cells has been documented using neutron diffraction [23,24], albeit the low flux of neutron sources means either the time resolution or the spatial resolution is severely limited. XRD studies have allowed more detailed maps of Lithiation across different cell formats to be done. Mattei et al. use high energy synchrotron X-ray diffraction to effectively map cathode SOC in NMC 622/Li metal cells with high sensitivity, though not done operando and with limited data on the corresponding anode [25]. Mühlbauer et al. use a combination of high-energy XRD and X-ray computed radiography to precisely map the lithiation state of corresponding $LiCoO_2$ cathodes and graphite anodes in a pouch cell at different states of charge, showing inhomogeneities in charge state of up to 10 percentage points, exacerbating degradation mechanisms [26]. The same group did similar studies on cylindrical cells, finding similar effects of inhomogeneities [27,28]. Recently, Charalambous et al. have revealed heterogeneities in Li inventory across single-layer pouch cells using lateral scanning XRD, showing a strong link between Li inventory inhomogeneity and cycling rate [29]. Operando XRD has been used on other battery applications too, where we have recently used high-energy XRD to map phase transitions in Zn-air battery electrodes spatially and in real time [30,31]. Given the increased volume expansion in full cells with Si–Gr anodes, and the highly anisotropic expansion of the particles in those anodes, it seems likely that the inhomogeneities observed during cycling of other Li-ion

battery chemistries may be exacerbated in this case, and could have an outsized effect on degradation of Si–Gr anodes.

In this work we investigate prototype NMC811/Si–Gr 5Ah multi-layered pouch cells manufactured by Cidetec, and use a combination of operando high-energy XRD and operando neutron diffraction, on the exact same set of cells in both pristine and aged states, to obtain complimentary and quantitative information on the behaviour of Si–Gr anodes in conjunction with NMC811 cathodes. Using the high flux synchrotron source at the DanMAX beamline at MAX IV, we can combine a good time resolution with a 2D mapping of the cell during operations, instead of measurements done at equilibrium at a few intermediate steps, allowing any inhomogeneities to be compared across electrodes in real time. Combining this with operando neutron diffraction allows the evolution of graphite phases during charge and discharge to be quantified. Combining 2D resolution with operando measurements on commercial-grade full-cells has to our knowledge not been done before using diffraction techniques, and has not been done with Si–Gr anodes.

2. Experimental methods

2.1. Pouch cells

The four 5 Ah multi-layer pouch cells studied here were manufactured and provided by Cidetec. The electrode format was 6 cm × 10 cm. All four cells were made with the same NMC 811 cathodes, and matched with either graphite or Si–Gr anodes (areal capacity balancing of 1.1 for anode/cathode). The loading of the cathodes was 3 mAh/cm^2, or 15.7 mg/cm^2 active material, while the anodes had a 3.3 mAh/cm^2 loading, corresponding to 9.9 mg/cm^2 for the graphite anodes, and 7.5 mg/cm^2 for the Si–Gr anodes. Each cell was made up of 15 double coated cathodes coated on Al, and 14 double coated and two single coated anodes coated on Cu. The total material weight was 24.094 g of cathode active material, 17.96 g of graphite in the Gr cells, and 12.24 g of graphite and 0.72 g of Si in the Si–Gr cells. The cathodes were manufactured with 90 wt% active material, 5 wt% C65 carbon black and 5 wt% PVDF, the graphite anodes were manufactured with 94 wt% graphite, 2 wt% C45 carbon black, 2 wt% W2000 5% and 2 wt% SBR 40%, and finally the Si–Gr anodes were made with 85 wt% of the same graphite used in the graphite anodes, 5 wt% Si, 3 wt% C45 carbon black, 3 wt% W2000 5% and 4 wt% SBR 40%. Formation cycles were performed by Cidetec following an internal proprietary protocol.

2.2. Electrochemical cycling

A NMC811/Gr and a NMC811/Si–Gr cell were cycled using a CC–CV step during charge (constant current followed by a constant voltage step), and CC during discharge. The CC current was 6 A (C-rate of 1.2). The cells were cycled between 2.8 V and 4.2 V. During CV, they were maintained at 4.2 V until they reached a current of 1 A. Both cells were cycled for a period of 20 days at 25 °C, with the Gr cell reaching 175 cycles, and the Si–Gr cell reaching 211 cycles. They reached a state of health (SOH) of 96% and 69% respectively. A Neware BTS4000 battery cycler was used. During operando experiments an Ivium CompactStat potentiostat was used to cycle the cells.

2.3. Neutron diffraction

Neutron diffraction studies were performed at the High-Resolution Powder Diffractometer for Thermal neutrons (HRPT) beamline at the SINQ neutron source, Paul Scherrer Institute (PSI) in Switzerland. The 3He (3.6 bar + 1.1 bar CF_4) multidetector consists of $25 \times 64 = 1600$ counters and a measuring range from 2θ angles 0° to 160°. The angular step size of 0.1° was reduced to 0.05° with the detector placed on air-cushions allowing intermediate steps to be sampled. The detector is 15 cm high, with a radius of 1.5 m, and an effective detection length of 3.5 cm [32].

Each cell was charged and discharged in the beam at 0.6 A for a full cycle, between voltage limits of 2.8 V and 4.2 V. Data was sampled continuously. When integrating the data into a 2θ diffractogram, the data was then binned over a time period of 7 to 30 min, with a trade-off between time-resolution and improved statistics. 90 min of exposure was done at a wavelength of 1.494 Å and the cell at a 45° angle to the beam, followed by 30 min of exposure with a wavelength of 1.155 Å and the cell at a 60° angle. The beam size was 1 × 2 cm^2, centred on the cell. Switching between these two configurations enabled the use of the highest possible flux allowed by the beamline for most of the scans, with the lowest background at low angles. The scans at a shorter wavelength, with the cell at 60°, in turn captured a larger portion of Q-space, albeit with less peak resolution.

The cells were clamped to a frame mounted on a vertical rod, on the beam and the detector (see figure 1 in supplemental information). The Gr cells were taped directly to the frame and cycled without externally applied pressure. The Si–Gr cells were clamped between two 1.5 mm Al plates, to prevent damage caused by expansion of the Si-containing anode.

2.4. X-ray diffraction

X-ray diffraction measurements were done at the DanMAX beamline at the 3 GeV synchrotron source at the MAX IV Laboratory. The DanMAX beamline has a high flux of 10^{12} ph/s at 35 keV, allowing low exposure times. A beamsize of 1×1 mm^2 was used. The DECTRIS PILATUS3 X 2M CdTe hybrid pixel array detector with a sample rate of up to 250 Hz, allowed ample sample time for fast scans across the batteries. Four cells were cycled operando, while the beam was scanned across a 10 by 61 point grid. This resulted in 610 diffractograms collected during each 12 min scan. Depending on the capacity of the cell, and thus the duration of each full charge/discharge cycle, the four operando measurements resulted in between 24400 and 47500 diffractograms per cell. During the operando measurements, the cells were clamped between two steel plates, with ten 65 mm vertical cut-outs spaced 10 mm apart (see figure 2 in supplemental material). X-ray was collected in these cut-outs. 2D data was integrated onsite using pyFAI.

2.5. Data analysis

For both X-ray and neutron diffraction data, Rietveld refinement was used to do a quantitative phase analysis of the NMC 811 cathode and the graphite phases in different lithiation states. This was done using Topas Academic (TA) v. 6.0 [33]. TA's native batch analysis tool allowed the use of a single input file to be used to sequentially refine all data for each cell. The diffractograms contained a strong Cu and Al signal from the 16 anode and 15 cathode current collectors, which were present and constant in all the collected diffractograms. By holding the scale factors and lattice parameters for Cu and Al constant throughout all the refinements, it was possible to obtain perfectly comparable data between cells, as well as accurately refine the sample–detector distance, crucial when working with a relatively large flat sample, moved perpendicularly to the beam.

When analysing the neutron data, sampled in a 2θ range, a correction was needed to account for the highly asymmetrical absorption profile of the flat sample. Here an asymmetric transmission correction described by Rowles et al. was used, to correct the relative intensities of the resulting diffraction peaks [34]. This approach enabled a quantitative Rietveld analysis to be done despite the shape of the pouch cell used.

A more detailed description of Rietveld refinement, as well as an example input file is included in supplemental information.

The calculation of x in Li_xC_6 is done from the weight percentages of the graphitic phases, and their relative lithium content. The phases LiC_{12} and LiC_6 are stoichiometric and contributes with a factor of 0.5

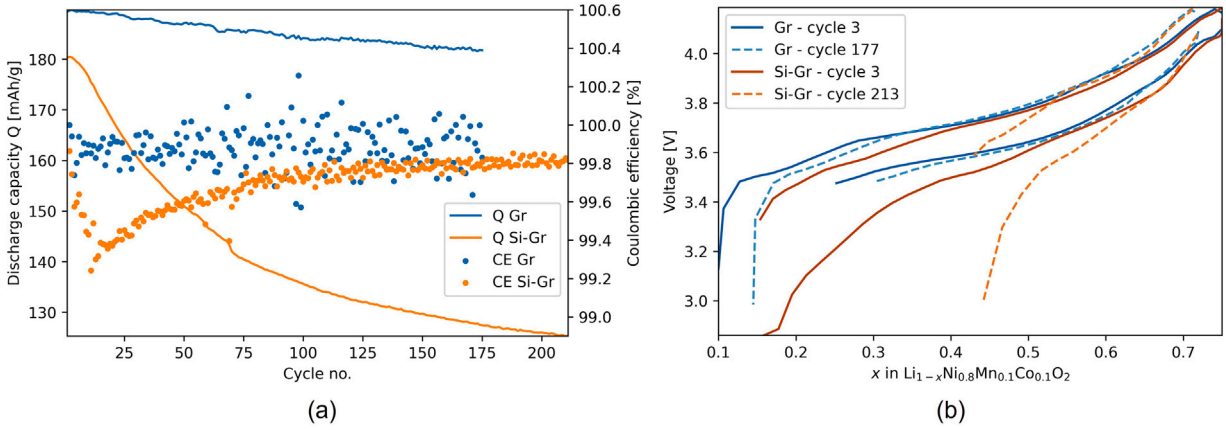

Fig. 1. (a) Capacity retention during discharge plotted alongside the coulombic efficiency, for a Gr cell and a Si–Gr cell. (b) Voltage profile as a function of x in $Li_{1-x}Ni_{0.8}Mn_{0.1}Co_{0.1}O_2$ pristine and aged Gr and Si–Gr cells. x calculated from operando XRD data, enabling a comparison of the lithiation state of the four cells' cathodes'.

(6/12) and 1 (6/6), respectively, to the total composition given as Li_xC_6. The refined "LiC_{18}" phase is a non-stoichiometric refined phase, representing the phases from almost no lithiation until stoichiometric LiC_{18} and contributes to the lithium content in the total composition Li_xC_6 with a factor relative to y in Li_yC_{18}. All phases with a lithiation degree up to LiC_{18} are refined with the LiC_{18} structure and the lithium content is estimated by assuming a Vegard's law dependence between the c-axes and the lithium content, i.e. a solid solution where the c-axis goes from 10.2 Å to 10.55 Å as the lithium content goes from 0 to 1. In the refinements, the unit cell parameter of graphite is confined to a narrow range with a c-axis of between 6.685 Å and 6.75 Å, and the low-lithiated phase was restricted to have a c-axis between 10.2 Å and 10.55 Å. As graphite is lithiated, the overall weight percentage of the graphite anode as a proportion of all material in the cell increases. This introduces a small error if only the relative weight percentages of the graphitic phases are taken into account, so this is normalised to the number of moles of C_6, as shown in the following equation;

$$x \text{ in } Li_xC_6 = \frac{3 \cdot \frac{y \cdot wp_{LiC_{18}}}{y \cdot M_{Li} + MC_{18}} + 2 \cdot \frac{wp_{LiC_{12}}}{M_{LiC_{12}}} + \frac{wp_{LiC_6}}{M_{LiC_6}}}{\frac{wp_{C_6}}{M_{C_6}} + \frac{wp_{LiC_{18}}}{y \cdot M_{Li} + M_{C_{18}}} + \frac{wp_{LiC_{12}}}{M_{LiC_{12}}} + \frac{wp_{LiC_6}}{M_{LiC_6}}}, \quad (1)$$

where y in Li_yC_{18} is given by

$$y = \frac{c - 10.2}{0.35} \quad (2)$$

3. Results

3.1. Electrochemical performance

The NMC811/Gr cell (referred to as Gr cell henceforth) has a fade rate of 2.3%/100 cycles over the full cycle test, while the NMC811/Si–Gr cell (referred to as Si–Gr cell) has an average fade rate of 14.4%/100 cycles (Fig. 1a). The Si–Gr cell degrades at an average fade rate of 30.2%/100 for the first 70 cycles and only 5.4%/100 cycles for the remaining cycles. A capacity of 0.93 Ah, or 21.5% of initial capacity, is lost during those first 70 cycles. The total capacity of the Si in the anode is 1.84 Ah. Assuming the graphite component of the anode undergoes a capacity fade similar to the graphite cell, around half of the available capacity from Si is lost after the first 70 cycles. The coulombic efficiency (CE) is low for the Si–Gr cell in the initial cycles, and gradually reaches the level of the Gr cell after 150 cycles. It seems clear from the significant degradation of the Si–Gr cell that Si has a large impact on the initial degradation of the cell, which is also clear from the low CE, related to the presence of an irreversible reaction.

3.2. Cathode performance and Li inventory

From refinement of diffraction data, lattice parameters and phase fractions of NMC811 (will be denoted NMC henceforth) and the different graphite phases have been obtained. The NMC a lattice parameter closely follows the lithiation of NMC, since the M-O binding length is close to linearly and inversely dependent on the Ni oxidation step, and can thus be used as a good proxy for state of charge of the cathode (SOC) and by extension x in $Li_{1-x}Ni_{0.8}Mn_{0.1}Co_{0.1}O_2$ (supplementary material Figure 3). Alternatively the unit cell volume can be used, but since the c-parameter falls dramatically when the cell reaches around 4 V, the volume is not linearly dependent on lithiation either (Figure 5 and 4 in supplemental materials). The a-parameter has thus been used to determine the lithiation state of the cathode in the different cells, relative to each other. In principle the Li-occupancy of NMC and graphite can be refined directly from neutron data, but with the low exposure times and thus low signal/noise ratio used here that was not possible to do accurately enough. The potential during charge and discharge plotted against x in $Li_{1-x}Ni_{0.8}Mn_{0.1}Co_{0.1}O_2$ is shown in Fig. 1b. The pristine Gr cell is close to the theoretical capacity with a charge capacity of 205 mAh/g, and is assumed to be fully lithiated $x = 0.1$ when discharged to 2.8 V and to be delithiated to $x = 0.75$ when charged to 4.2 V, consistent with the study by Marker et al. regarding NMC81 [35]. The NMC a-parameter for the pristine Gr cell in the charged and discharged state has then been used to define $x = 0.1$ and $x = 0.75$, in turn allowing the three remaining cells to be plotted on the same scale. In contrast to the pristine Gr cell utilising the full Li range, the three other cells operate in a narrower range.

The pristine Si–Gr cell (3 cycles after formation, no. 2 being during the operando neutron experiment) reaches the same delithiation state at the upper potential as the pristine Gr cell, as would be expected since the cathodes are identical. In the pristine cathode, Li can be accessed and extracted fully during charge, and there is enough Li available in the cell to fully lithiate the cathode during discharge. There is a clear difference in the potential profile at $x < 0.5$ however, which reflects a different potential on the anode side. The total capacity of the Si–Gr cell is however lower than the Gr cell, which is visible at low x values. This is also visible from the cycling data shown in Fig. 1a, where the initial cycles are 20 mAh/g lower for Si–Gr than Gr. The formation cycles are not included here, but the difference is due to a larger initial loss of Li to the SEI layer on the anode.

After 177 cycles (175 + 1 + 1; cycling + operando neutron + operando XRD), the Gr cell has lost 4.04% of its initial capacity. From Fig. 1b it is apparent that about $x = 0.04$ of that lost capacity happens at high potential, with the cathode not being fully delithiated, while the lost $x = 0.05$ at lower potential shows that the cathode is not being fully re-lithiated during discharge.

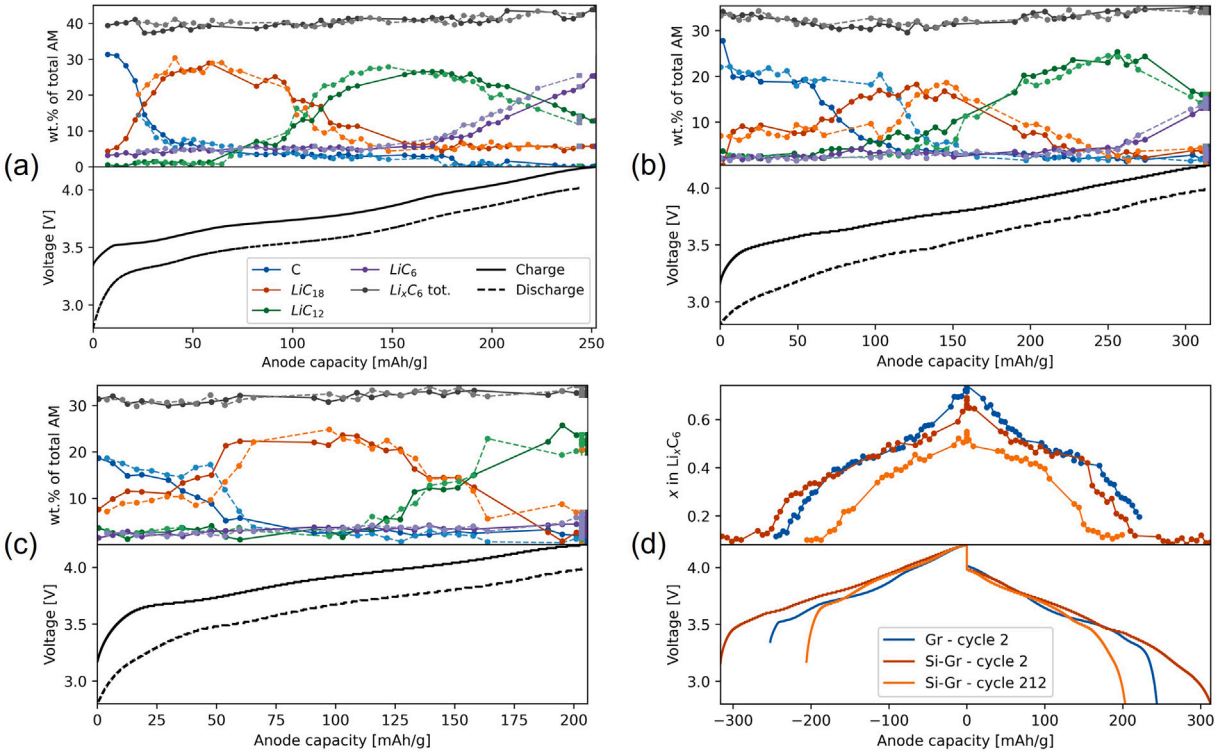

Fig. 2. Graphite phase fractions as percentage of total active material alongside voltage profiles, calculated from neutron diffraction. Plotted as a function of gravimetric anode capacity. The total wt.% of all graphitic phases Li_xC_6 is also included for reference (a) Gr cell at cycle 2, (b) Si–Gr cell at cycle 2, (c) Si–Gr cycle at cycle 212. (d) Lithiation state of graphite component in the different cells, calculated from the relative weight percentages shown in (a)–(c).

After 213 cycles (211 + 1 + 1), the Si–Gr cell has lost 30.75% of its initial capacity. The cathode reaches the same state of delithiation as its Gr counterpart, but loses significantly more when lithiated.

3.3. Lithiation of Si and Graphite components in the anode

Using X-ray and neutron diffraction it is possible to detect the presence of the different phases graphite undergoes when lithiated, beginning with pure graphite, transitioning to LiC_{24} and LiC_{18} with an increasing Li content and correspondingly changing unit cell volume, then transitioning to LiC_{12} before ultimately reaching the fully lithiated LiC_6 phase. LiC_{24} is difficult to refine using Rietveld refinement, so is in effect captured in the LiC_{18} signal, meaning that LiC_{18} is not stoichiometric to begin with [36]. "Graphite" will be used forthwith to describe the anode as a whole in all its phases, any reference to the graphite in its delithiated form will be mentioned as the graphite phase. Once all graphite has reached the LiC_6 phase, any further attempt at lithiation would result in Li-metal plating on the surface of the graphite anode. The aforementioned graphite-derived phases manifest themselves in a single reflection in the X-ray diffractograms. In the neutron patterns far more graphite reflections are visible, enabling a potentially more accurate refinement of the different graphite phases, and thus a more accurate determination of relative weight percentages and lattice parameters.

3.3.1. Describing different graphite derived phases

In the Figures shown in Fig. 2 the weight percentage (wt.%) of the four main graphite phases are shown for the pristine Gr cell (Fig. 2a), the pristine Si–Gr cell (Fig. 2b), and for the aged Si–Gr cell (Fig. 2c), as well as the total lithiation of the graphite component of the anodes in Fig. 2d. Due to an unfortunate beam dump during the neutron experiment, no data were collected on the aged Gr cell. The weight percentages shown are percentages of the diffraction signal from active material in the cell, ie. NMC and graphite. The voltage profiles are plotted against the gravimetric capacity of the anode. All the cells begin with graphite in its fully delithiated form. The x in Li_xC_6 is calculated by summing the contributions from each of the phases LiC_{18}, LiC_{12} and LiC_6, based on the weight percentages. The LiC_{12} and LiC_6 phases are stoichiometric, while LiC_{18} behaves as a solid solution and goes from pure graphite to LiC_{18}. As this happens the unit cell expands, and the c lattice parameter changes. This is used to determine the contribution from LiC_{18} to the total lithiation in graphite. The calculation used to determine x is given in Eq. (1).

The Gr cell in Fig. 2a begins with 32 wt% graphite, with the two Si–Gr cells beginning at 27 wt% and 20 wt% graphite. The total wt.% of all the graphitic phases present is also shown and corresponds very closely to the actual graphite content in the assembled cell. The Si–Gr cells were assembled with 35 wt% graphite (Li_xC_6 tot.), and the Gr cells with 42 wt%, here the measured proportions are 32 wt% and 40 wt%.

For the Gr cell an immediate onset of graphite lithiation is observed as the graphite wt.% drops off almost immediately (Fig. 2a), as LiC_{18} rises. At around 100 mAh/g the phase fraction of LiC_{12} begins rising and constitutes the totality of the graphite at around 150 mAh/g, or 60% of the charge capacity. It in turn gives way to LiC_6, such that when the Gr cell is fully charged, LiC_6 reaches 27 wt%, with LiC_{12} at 14 wt%, and a total lithiation of $x = 0.77$ in Li_xC_6 (Fig. 2d). Since the anode/cathode balance is 1.1, it makes sense that the anode is not fully lithiated when the cell is charged. The process during discharge very closely follows the charge process in reverse.

In the Si–Gr cell at cycle 2 in Fig. 2b the graphite signal remains unchanged until around 60 mAh/g, with the rise in LiC_{18} signal delayed accordingly. LiC_{12} reaches its peak at 25 wt% after 250 mAh/g, as LiC_6 begins to appear. At cutoff, the graphite in the anode is less lithiated than in the Gr cell, with $x = 0.65$ in Li_xC_6 (Fig. 2d), apparent by the lower proportion of LiC_6 relative to LiC_{12} (Fig. 2b). During discharge, the delithiation of LiC_6 and LiC_{12} follows the lithiation in reverse. A significant asymmetry is however apparent as LiC_{18} begins delithiating around 40 mAh/g earlier than during charge, with graphite

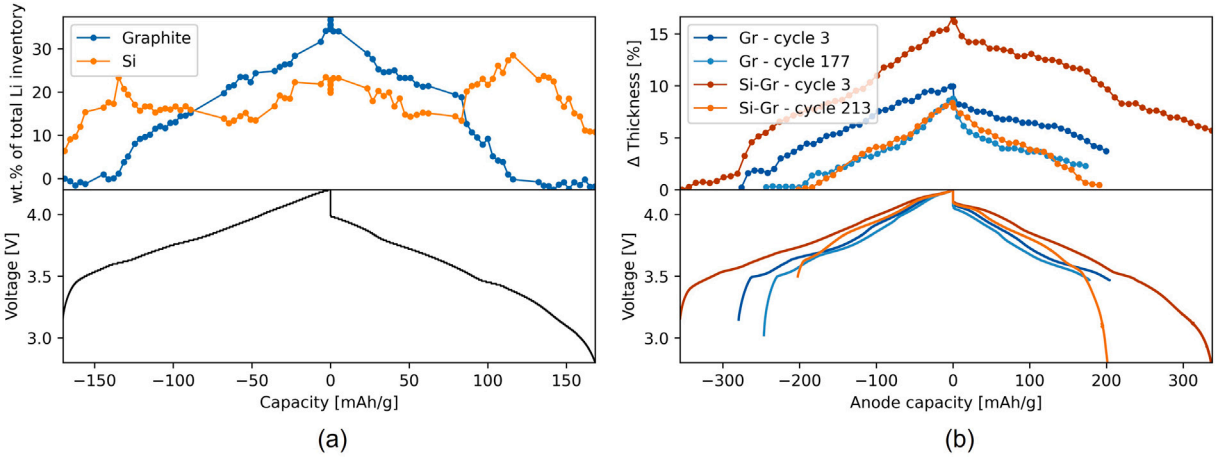

Fig. 3. (a) From neutron diffraction data. Si and graphite behaviour in the anode of a Si–Gr cell at cycle 2, calculated from the lithiation state of graphite in the pristine Si–Gr cell and the pristine Gr cell. Plotted as a function of gravimetric cathode capacity. (b) From XRD data, volume change as Δ thickness for all four cells. Plotted as a function of gravimetric anode capacity.

likewise reappearing at this earlier stage. Since the wt.% of graphite is practically constant at low anode capacities, it is clear here that alloying and dealloying of Li and Si must account for the first 70 mAh/g of capacity during charge, and last 110 mAh/g during discharge.

For the Si–Gr cell at cycle 212 (Fig. 2c), the picture is similar to cycle 2, but with an earlier onset of graphite lithiation (40 mAh/g versus 70 mAh/g for the pristine cell), and less hysteresis between charge and discharge, with only 10 mAh/g difference between the phase transition from LiC_{18} and graphite during charge and discharge. When the cell is fully charged the LiC_{12} phase dominates, with a total lack of LiC_6, and thus a final lithiation of the graphite component of the anode of $x = 0.55$ in Li_xC_6. It is interesting to note that the graphite in the aged Si–Gr anode is not fully delithiated when discharged (Fig. 2d), indicating kinetic limitations preventing full delithiation of graphite particles. Unfortunately no neutron data was collected on the aged Gr cell, to compare the degradation independent of any cross-talk effect with Si.

3.3.2. Lithiation of graphite and Si

By combining the information from relative weight percentages of the different graphite phases, it is possible to calculate the total lithiation state of graphite in the anode. In the Gr cells this corresponds to the lithiation state of the full anode, while in the Si–Gr cells it enables the role of Si to be inferred from the difference between the Gr and Si–Gr cells. Since the total mass of NMC is constant across all cells, and known precisely, the NMC wt.% is used to calculate the final weight of Li in graphite, assuming that the measured spot is representative for the full cell. The lithiation state of graphite is then calculated from the total weight of available Li known to be in the cell, representing the stoichiometric Li contained in the 24.095 g of NMC in the cell on assembly, ie. 1.72 g of Li per cell.

The alloying of Li and Si is difficult to detect directly with diffraction techniques, since Li_xSi forms an amorphous structure after the initial formation cycle. By comparing the lithiation patterns of the Gr and the Si–Gr cells at cycle 2 shown in Fig. 2d, the lithiation path of the Si component can be inferred. This has been done in Fig. 3a. The blue line shows the Si–Gr cell at cycle 2, while the orange line shows the wt.% of the total Li inventory in the pristine Si–Gr cell subtracted from than in the pristine Gr cell. This is possible since the two cells are in their pristine state and have identical cathodes. The wt.% of the total Li inventory should add up to 89%, on account of the percentage of the initial capacity obtained. In Fig. 3a it adds up to around 57% when the cell is fully charged, indicating that all the Li is not accounted for. Qualitatively the results show that Si is lithiated from the onset, while the lithiation of Gr is delayed. After 40 mAh/g, Gr takes over, and after an initial rapid rise, slowly increases until the cell is charged. The Si component lithiates at a slightly lower rate. During discharge there is a clearer separation between Gr and Si, with delithiation predominantly happening in Gr until after 116 mAh/g, with Si then delithiating in the final stages of discharge.

3.4. Volume expansion

X-ray diffraction enables the detection of very small changes in diffraction angles from different crystal planes. This provides the sensitivity to detect changes in unit cell lattice parameters in the order of a few thousands of an Ångstrøm. The set sample–detector distance is used to calculate the diffraction angles from the crystalline sample, so a change in sample displacement can thus be separated from a change in unit cell parameters since its angular dependency is different from that of the Bragg reflections, described in the literature [37–39]. The presence of identical Al and Cu current collectors in all the cells, inactive components with strong diffraction signals that can be used as references, allows the displacement of the sample to be refined with precision, and changes in displacement to be compared between cells. The cells were securely fastened to the sample stage, so the change in displacement observed has been interpreted as a change in the thickness of the sample. This technique is different from profilometry in that it does not look at the displacement of the surface of the cell, but rather the average displacement of all the crystalline material within the 5 mm (thickness of the cell) × 1 mm × 1 mm volume exposed in each of the 610 grid points. With a total of 32 electrodes, the local non-planarity of individual electrode layers should not affect the overall picture within each pixel. An overall tilting of the cell and sample holder relative to the detector plane would express itself in a clear shift in the constant diffraction peaks from Al and Cu, within the first scan before the initial charge. This was not the case. The resulting change in thickness as a percentage of the initial thickness is shown in Fig. 3b, and the maximal change over the surface of the cells is shown in Fig. 4. (Calculation detailed in supplemental material).

Purely based on the amount of NMC and Gr present in the cell, the Gr cell should expand by 7%, and the Si–Gr cell by 12%. If the expansion happened anisotropically this would signify an increase in thickness of 0.4% and 0.5%, not taking into account any reduction in porosity resulting from compression of the carbon black and binder present in the anode. In this case the constraints of the cell housing must signify that the expansion predominantly happens normally to the current collectors. The two Gr cells expand by 10% during charge, while the pristine Si–Gr cell expands by 17%.

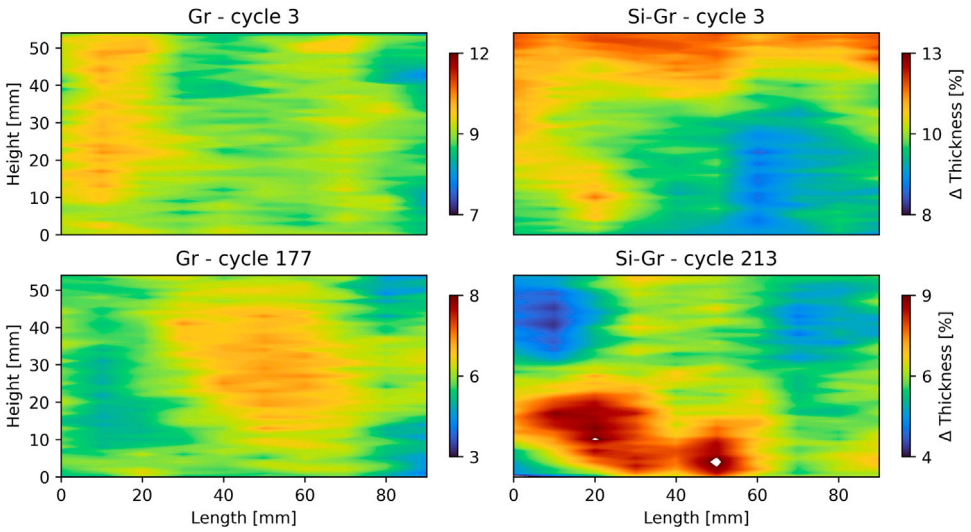

Fig. 4. From XRD operando lateral scans. Thickness variation across each cell when fully charged, shown as % of the starting thickness. Colour bars all show the same range of Δ 5%, centred around the mean value for each cell. (For interpretation of the references to colour in this figure legend, the reader is referred to the web version of this article.)

The heatmaps in Fig. 4 show the maximum cell thickness, when the cells are fully charged. The scales of all four heatmaps all show the same range of Δ 5%, centred around the mean value, such that inhomogeneity across the cell can be compared easier from cell to cell. Both Gr cells expand significantly, but homogeneously. After 3 cycles there is little variation across the cell, whereas at cycle 177, the centre expands significantly more than the edges, albeit still 29% less than in the pristine state. The Si–Gr cells expand in the same order as the Gr cells, but less homogeneously. At cycle 3 there seems to be an edge effect, with more expansion along the upper edge of the cell. In the aged cell after 213 cycles, there are two under-expanded areas (blue patches), as well as an area that sees significantly more expansion than the rest (dark red patch), ie. closer to the level of thickness expansion seen in the pristine Si–Gr cell.

3.5. Lithiation inhomogeneity across cathode and anode

The 2D maps obtained from the continuous scans across the four pouch cells during operation made it possible to gauge any inhomogeneity in lithiation in the cathode and the anode during operation. Using Rietveld refinement, and using the resulting lattice parameters as well as phase fractions, the lithiation of the NMC cathode and the graphite component of the anode have been mapped. They are shown here as x in $Li_{1-x}Ni_{0.8}Mn_{0.1}Co_{0.1}O_2$ for NMC, and x in Li_xC_6 for graphite.

The 610 diffractograms collected every 12 min have enabled the creation of between 44 and 76 2D maps during a full cycle, corresponding to between 4.5 and 2.7% of the total charge capacity. Each 2D map is thus also spread in time, with 12 min between the scan taken in the first corner and the last. A 4% variation in state of charge across the heatmap is very visible, and may obscure any spatial inhomogeneity due to other effects. To address this in the heatmaps showing x in $Li_{1-x}Ni_{0.8}Mn_{0.1}Co_{0.1}O_2$ for the cathode and x in Li_xC_6 for the graphite component of the anode, a linear correction has been applied, corresponding to the x difference between the timestamp of the first and last diffractogram in a 2D scan. The heatmaps of the cells are taken while they are still charging, avoiding any redistribution of charges at equilibrium. The heatmaps in Figs. 5 and 7 when nearly fully charged are taken before they reach cutoff, meaning that a red-shift shows areas more active than blue shifted areas. The opposite is the case in Figs. 6 and 8, where a blue shift shows the most active areas leading the discharge. The heatmaps are interpolated across the 610 "pixels" constituting each image.

3.5.1. Cathode lithiation

As was shown in Fig. 1b, there is a large difference in how much the cathode can be lithiated during discharge, reflecting large reductions in Li inventory. Fig. 5 shows x in $Li_{1-x}Ni_{0.8}Mn_{0.1}Co_{0.1}O_2$ just before the cell is fully charged, while Fig. 6 shows the same cells just before they are fully discharged. All the heatmaps during charge in Fig. 5 are plotted with the same range of $x = 0.026$, and during discharge in Fig. 6 with a range of $x = 0.042$, centred around the mean x value for each cell, to make differences in inhomogeneity across the cells visible.

Looking first at the Gr cells, the cell at cycle 3 is homogeneously charged and discharged, while after 177 cycles during charge the edges are about $x = 0.01$ ahead of the centre of the cell (Fig. 5). The pristine Si–Gr cathode lithiation is as homogeneous as the Gr cell, while the aged Si–Gr cell is far more inhomogeneous, with the centre of the cathode over $x = 0.02$ behind the edges during charge (Fig. 5), and over $x = 0.04$ when discharged (Fig. 6). The aged Si–Gr cell is clearly less active in the centre of the cell, with a more pronounced effect than in the less degraded Gr cell. There are however notable spots of high lithiation in the centre of the cell, amongst the areas of higher lithiation (green spots in the middle of Fig. 6, bottom right frame).

3.5.2. Anode lithiation

The graphite lithiation has been calculated as in Fig. 2d for neutrons, but using the available XRD data. The absolute values are less precise than the neutron data, but the relative differences across the cell are still accurate. The heatmaps in Figs. 7 and 8 show the charge and discharge of the graphite component of the anode as x in Li_xC_6. The total lithiation expressed as x in Li_xC_6 only shows a partial picture of the inhomogeneities across the cell, and relative changes in phase composition. To accurately represent this aspect, heatmaps at the same point in time as those shown in Figs. 7 and 8 are shown in Supplemental materials. In the case of the Gr cell, the cell at cycle 3 shows a fairly large inhomogeneity in x during charge (Fig. 7), but less so during discharge. In the aged Gr cell, x during charge is more homogeneous, while clearer inhomogeneities with a range of x=0.15 are visible during discharge (Fig. 8). The heatmaps of the Gr cell anodes during discharge are at a SOC of around 28% (relative to a slow cycle of the pristine Gr cell), due to the premature termination of the experiment during the final discharge of the cells. The x values are thus correspondingly high. The Si–Gr maps during discharge (Fig. 8) are shown to correspond to a similar SOC. As was the case with the cathode, the Li inventory in the pristine Si–Gr cell is very homogeneous during (de)lithiation, while significant heterogeneities across the electrodes are visible for the aged

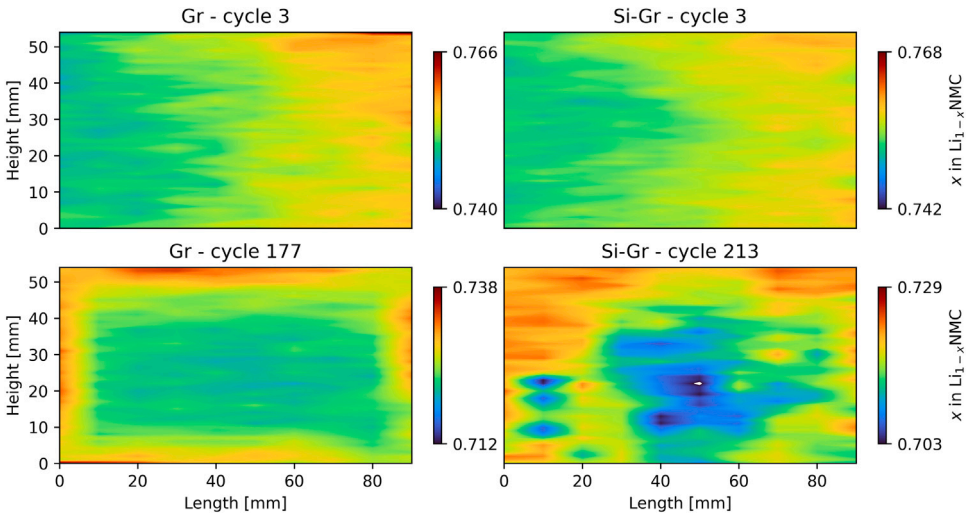

Fig. 5. Heatmap of x in $Li_{1-x}Ni_{0.8}Mn_{0.1}Co_{0.1}O_2$ during charge. These heatmaps are captured towards the end of the charge cycle, before reaching cut-off potential. Red-shift shows areas more active than blue-shifted areas. Colour bars all show the same range of $x = 0.026$, centred around the mean value for each cell, to ease comparison of inhomogeneity between cells. (For interpretation of the references to colour in this figure legend, the reader is referred to the web version of this article.)

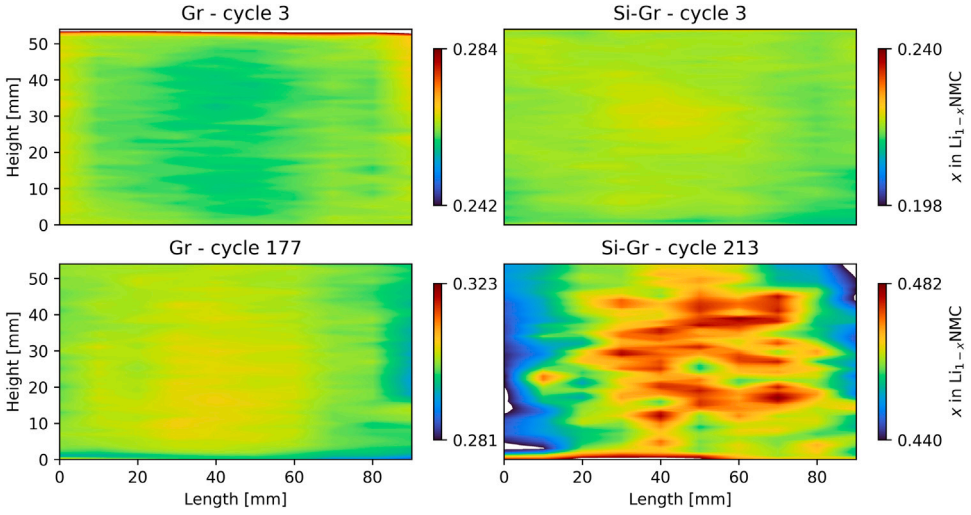

Fig. 6. Heatmap of x in $Li_{1-x}Ni_{0.8}Mn_{0.1}Co_{0.1}O_2$ during discharge. These heatmaps are captured towards the end of the discharge cycle, before reaching cut-off potential. Blue-shift shows areas more active than red-shifted areas, as the blue-shifted areas here are more discharged. Colour bars all show the same range of $x = 0.042$, centred around the mean value for each cell, to ease the comparison of inhomogeneity between cells. (For interpretation of the references to colour in this figure legend, the reader is referred to the web version of this article.)

Si–Gr cell. In the aged Si–Gr cell there is a tendency for more irregular inhomogeneity in graphite lithiation than was the case in the cathode. There are local areas with variations of up to $x = 0.25$ (Fig. 8, lower right frame). When considering individual phases, it is apparent that the centre of the cell has a strong LiC_{12} (Figure 8 in SI) and graphite signal, while it has a lower LiC_{18} signal (Figure 7 in SI). Areas with remaining LiC_6, which are thus most inactivated, are distributed across the cell (Figure 9 in SI).

4. Discussion

4.1. Lithium inventory

One of the main reasons the Si–Gr cells rapidly lose capacity is a reduction in the amount of available and cyclable Li^+. This is evident from four factors:

Firstly, the Si–Gr cell degrades at a rate of 30.2% per 100 cycles for the first 70 cycles (Fig. 1a). Once that capacity has been lost in the second part of cycling, once the fade rate of the Si–Gr cell has stabilised (Fig. 1a), the cell subsequently degrades slower, with a degradation rate closer to that of the Gr cell. The fall in capacity is in part due to polarisation, shown by the fact that the cell subsequently recovers a large part of its capacity when cycled slowly during the operando experiment. The low CE of the Si–Gr cell compared to the Gr cell initially indicates the presence of an irreversible reaction. The CE rises gradually and ends up close to that of the Gr cell in the later cycles, which is due to Si becoming largely inactive.

Secondly, capacity loss on the cathode side happens at high lithiation states, i.e. when $x < 0.4$ in $Li_{1-x}Ni_{0.8}Mn_{0.1}Co_{0.1}O_2$ (Fig. 1b). The cathode is still fully active, but a lack of Li inventory prevents the cathode from being lithiated sufficiently during discharge. The potential of the different cells at $x > 0.55$ during charge and $x > 0.65$ during discharge (Fig. 1b) shows that the degraded Si–Gr cell is not operating with an increased overpotential when charged, so the loss in capacity has not affected the kinetics on the cathode side to the extent that can account for the capacity loss. Marker et al. [35] notice the kinetics of extracting the last Li^+ ions from the cathode worsening when cycling cells to 4.4 V vs Li^+, contrary to when they are cycled to 4.2 V as

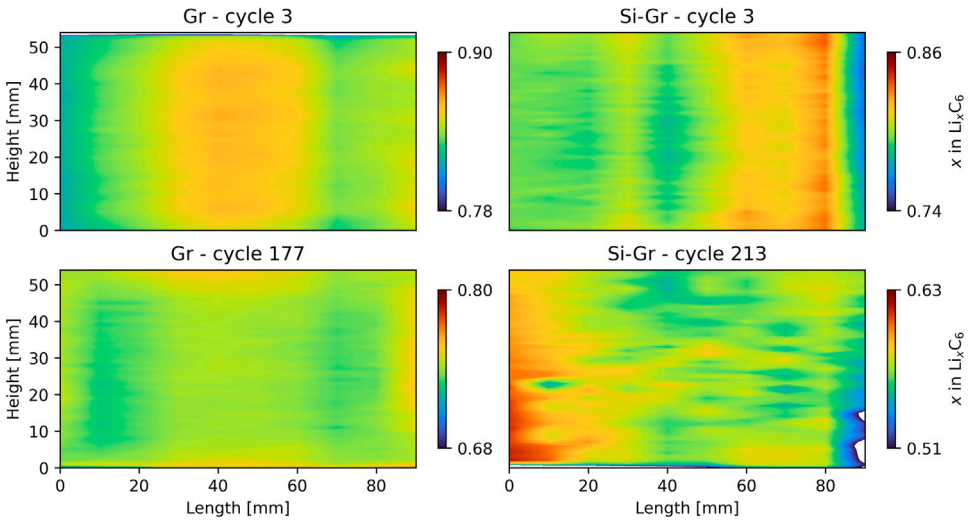

Fig. 7. Heatmap of x in Li_xC_6 during charge. These heatmaps are captured towards the end of the charge cycle, before reaching cut-off potential. Red-shift shows areas more active than blue-shifted areas. Colour bars all show the same range of $x = 0.14$, centred around the mean value for each cell, to ease the comparison of inhomogeneity between cells. (For interpretation of the references to colour in this figure legend, the reader is referred to the web version of this article.)

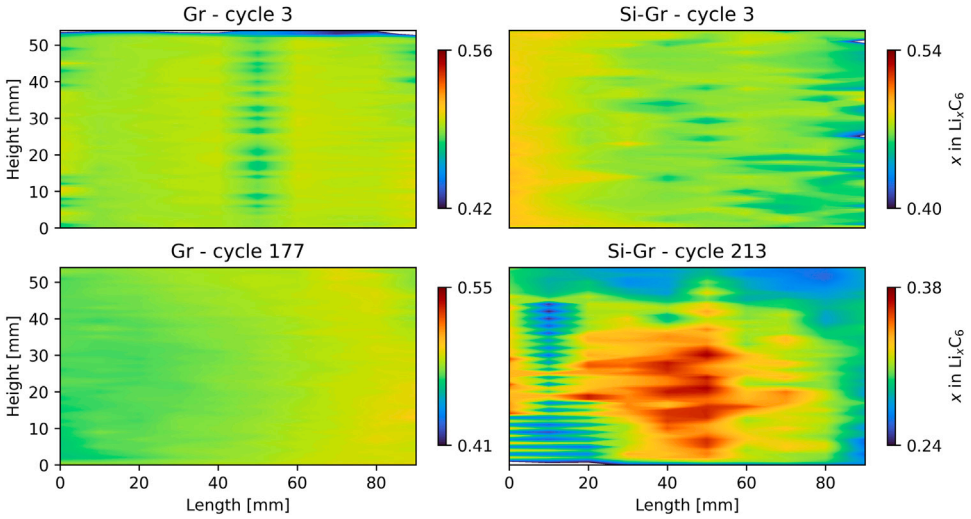

Fig. 8. Heatmap of x in Li_xC_6 during discharge. These heatmaps are captured towards the end of the discharge cycle, before reaching cut-off potential. Blue-shift shows areas more active than red-shifted areas, as the blue-shifted areas here are more discharged. Colour bars all show the same range of $x = 0.26$, centred around the mean value for each cell, to ease the comparison of inhomogeneity between cells. (For interpretation of the references to colour in this figure legend, the reader is referred to the web version of this article.)

is the case here. There is an increase in overpotential during discharge (Fig. 1b) arising when Li^+ becomes difficult to extract from the anode. The kinetic limitations leading to this increase in overpotential could be due to the disconnection of graphite particles from the conductive network within the anode.

Finally, the graphite on the anode side also operates at low lithiation. The significant reduction of available Li^+ seen from the cathode delithiation is visible in the neutron diffraction data of the aged Si–Gr cell (Fig. 2c) as a lack of any LiC_6 signal when the cell is fully charged.

Most of the missing Li^+ is not intercalated in inactivated NMC or graphite. About $x = 0.04$ is left in the centre of the NMC cathode when fully charged (Fig. 1b), and $x = 0.15$ is left in the graphite component of the anode when the cell is fully discharged (Fig. 2d). Likewise any inactivated LiC_6, LiC_{12}, as well as inactive graphite preventing further intercalation, would remain visible in the phase fraction Figures in Fig. 2. The $x = 0.04$ that remains intercalated in NMC at $x > 0.7$ in $Li_{1-x}Ni_{0.8}Mn_{0.1}Co_{0.1}O_2$(Fig. 1b) happens both in the aged Gr cell and aged Si–Gr cell, and is most likely due to the slight overpotential resulting in the cell hitting the upper cut-off voltage of 4.2 V prematurely. The remaining Li^+ could probably have been extracted with the inclusion of a CV step, or a higher cutoff voltage, [35] and would be worth investigating in a future experiment.

Since the graphite component of the Si–Gr anode operates similarly to that of the graphite in the Gr cells, and the graphite has lost little capacity compared to the overall capacity of the cell (Fig. 2d), the SEI layer formed around the graphite particles is unlikely to be more extensive than in the Gr cells. This means that the lost Li^+ must either be alloyed to inactivated Si, be incorporated in an increasingly large SEI layer around the Si particles, or trapped in the centre of Si particles, as proposed by Moon et al. [18].

4.2. Deconvoluting graphite (de)lithiation and Li alloying of Si particles

The alloying of Si relative to the lithiation of graphite can be inferred by comparing Gr and Si–Gr cells. The (de)alloying of Si and Li does not directly follow the (de)lithiation of graphite. This can be seen from the following three factors :

Firstly, on the voltage profile for the pristine Si–Gr cell in Fig. 1b the potential difference between charge and discharge is markedly different, with the potential dropping off during the end of discharge, a very visible departure from the pattern of the Gr cell.

Secondly, the relationship between graphitic phase fractions during charge and discharge for the Si–Gr cell (Fig. 2b) shows very clearly that the onset of graphite lithiation comes at a much lower capacity than the delithiation during discharge, meaning that although Si alloying begins before graphite lithiation, during discharge Si dealloying is dominant for the last 45% of the discharge, with graphite being completely delithiated early on (Fig. 2b).

And finally, lithiation of the graphite anode in the Gr cell tops out at $x = 0.75$ in Li_xC_6 (Fig. 2d), meaning that 72% of the available 1.72 g of Li originating in the cathode can be accounted for in the graphite anode. The graphite component of the anode in the pristine Si–Gr cell contains 43.3% of the same amount of Li when fully charged. The discrepancy between the two is partly due to the slight capacity difference, but is otherwise a clear effect of the Si in the anode, as was observed in Fig. 2. The slow initial lithiation of graphite is visible in Fig. 2d. After 213 cycles the Si–Gr cell has lost 36% of its initial capacity, but only 22% of the available Li^+ in graphite.

The Si and Gr contributions are deconvoluted in Fig. 3a. Heubner et al. [8] found that during lithiation of the anode, alloying of Li and Si dominated at anode potentials above 220 mV. Below that threshold, graphite and Si alternately take over the reaction, leading to both components increasing in Li content. The anode potential was not measured here, but the from Fig. 3a, this would be a good explanation. Heubner et al. describe that the asymmetry during discharge arises because of a larger potential hysteresis for Si than graphite, with Si mainly delithiating at anode potentials above 450 mV [8]. This would match the results in Fig. 3a, with the Si level staying close to constant until graphite is completely delithiated. Heubner et al. showed this asymmetry very well in their “model-like blended electrode”, but quantitative analysis in commercial-type electrodes and full cells is essential to validate that the mechanism is similar in actual blended electrodes. The asymmetry was shown by Berhaut et al. using small angle X-ray Scattering [40]. but was less visible in the data presented by Moon et al. [18], where the discharge to a much larger degree resembles the charge pattern.

4.3. Effect of electrode-wide inhomogeneity on Si–Gr anode degradation

The Li inventory across the pristine pouch cells during charge/discharge is very homogeneous, while inhomogeneity in local Li inventory across the electrodes is visible in the aged cells. For the Gr cells there is up to a $x = 0.1$ difference between the centre of the electrode and the edges the cathode. This is particularly visible in the Gr cell at cycle 177, on the cathode during charge (Fig. 5). The Si–Gr cell at cycle 213 has a $x = 0.25$ range on the graphite component of the anode (Figs. 7 and 8), and a range of $x = 0.02$ during charge (Fig. 5 and $x = 0.04$ during discharge Fig. 6). The inhomogeneity across the anode is thus ten fold larger than in the cathode, which could be an inhomogeneous effect of Si.

In all the cells, the edges of the cells perform better than the centre. This could be due to several factors. (1) It has been reported that in cylindrical 18650 cells, electrolyte has a tendency to be depleted in the centre of the cell and remain in the outer layers, and is directly linked to loss of Li^+ [28]. A similar effect could be happening here, with electrolyte being depleted in the centre of the pouch cell perhaps being incorporated in a larger SEI layer locally. This would increase the local overpotential, and thus explain a SOC lower than the mean across the electrode. (2) The pouch cells are cycled while clamped between two plates. During preliminary cycling the cells were clamped between 2 mm plexiglas plates. The plates were not completely rigid, and may have permitted more expansion in the centre of the cell than along the edges, in turn decreasing internal contact in the centre of the cell. The thickness change in the pristine Si–Gr cell shown in the upper right of Fig. 4 shows the effect that an unevenly clamped cell can most likely have on expansion, with the cell expanding significantly more along one edge. (3) Charalambous et al. show that high C-rates result in seemingly random inhomogeneities across single layer pouch cells, but that degraded cells tend to lose activity in the centre of the cell [29], an effect that is especially seen here on the cathode side on the degraded Si–Gr cells.

XRD provides a way to map volume expansion of a cell in 2D operando, while still clamping the cell between two plates. Expansion of Si particles has been shown to have a large impact on capacity suppression of graphite in blended Si–Gr electrodes [18]. Since the aged Si–Gr cell shows significant inhomogeneity in graphite (de)lithiation it stands to reason that there could be a spatial component to the suppression of capacity in graphite. The performed lateral mapping shows that the volume expansion in the centre of the aged Si–Gr cell (Fig. 4, bottom right) broadly coincide with the least active areas of the graphite component of the Si–Gr electrode (Figs. 7 and 8).

The expansion seen here (Fig. 3b) is very large considering that if the particles expand anisotropically, the expansion in 1D would theoretically be under 0.5%. Gas evolution within the cell could also lead to an expansion of the cell. Since the expansion is largely reversible, however, the dominant effect observed here is unlikely to be due to gassing and bubble creation, which would result in a permanent expansion. These results are consistent with other authors who describe that graphite anodes have a tendency to expand in a highly anisotropic manner, with reported expansion of Gr electrodes of 6%–7%, with particle expansion of 10%. They also observe highly anisotropic expansion of Si–Gr electrodes, despite the isotropic nature of the Si particle expansion [14], similar to the results shown here. Others observe an expansion in the order of 10%–15% of pouch cells with Si–Gr anodes [18]. The method shown here adds an extra 2D areal aspect, enabling simultaneous operando measurement of local volume change, and lithiation of both electrodes.

5. Conclusions

Four prototype 5 Ah multi-layer pouch cells with NMC811 cathodes and either graphite or silicon–graphite anodes have been studied using operando neutron diffraction and operando X-ray diffraction. One Gr and one Si–Gr cell were degraded beforehand. It was demonstrated that high-quality neutron diffraction data could be obtained without using a deuterated sample, and that a quantitative Rietveld analysis could be performed despite the geometrical shape of the sample resulting in a highly asymmetrical absorption profile.

It was found that the predominant factor behind capacity fade in Si–Gr cells is loss of Li inventory to Si. The graphite component of the anode and the NMC811 cathode continue to operate with little change in available capacity and overpotential, meaning that they are not the limiting factor. The Si present in the blended anode is largely inactivated during the initial 70–100 cycles.

The alloying of Si and the lithiation of graphite happens at different rates, in an asymmetrical way during charge and discharge. It was found that Si alloying dominates early on during charge at higher anode potentials, with graphite and Si both contributing to anode capacity in the later charge stages. During discharge, the two are more clearly separate, with graphite being nearly fully delithiated before the de-alloying of Li and Si begins.

By using the high X-ray flux and the fast detector at the DanMAX beamline at MAX IV, combined with a rapidly moving sample stage, up to 76 2D maps of the pouch cells could be obtained during a full cycle, enabling quantitative phase mapping across a 2D area to be done. Here it was observed that SOC inhomogeneity increased significantly with degradation in the Si–Gr cells. There was up to 20% SOC difference across the graphite in the anode, and 5%–6% SOC variation across the cathode, despite the cathode itself not being very degraded. On both

electrodes the edges of the cell remained more active than the centre, presumably because of an increased expansion and pressure build-up. XRD data was also used to track the cell expansion operando, and map that expansion across the cell, linking it to electrode lithiation states.

CRediT authorship contribution statement

Kristoffer Visti Graae: Conceptualization, Methodology, Writing – original draft, Writing – review & editing, Investigation, Formal analysis. **Xinyu Li:** Investigation, Writing – review & editing. **Daniel Risskov Sørensen:** Investigation, Writing – review & editing. **Elixabete Ayerbe:** Investigation, Writing – review & editing. **Iker Boyano:** Investigation, Writing – review & editing. **Denis Sheptyakov:** Investigation, Writing – review & editing. **Mads Ry Vogel Jørgensen:** Investigation, Writing – review & editing. **Poul Norby:** Supervision, Conceptualization, Methodology, Investigation, Writing – review & editing.

Declaration of competing interest

The authors declare that they have no known competing financial interests or personal relationships that could have appeared to influence the work reported in this paper.

Data availability

Data will be made available on request.

Acknowledgements

This work is based partly on experiments performed at the Swiss spallation neutron source SINQ, Paul Scherrer Institute, Villigen, Switzerland. We acknowledge MAX IV Laboratory for time on Beamline DanMAX under Proposal 20211062. Research conducted at MAX IV is supported by the Swedish Research council under contract 2018-07152, the Swedish Governmental Agency for Innovation Systems under contract 2018-04969, and Formas under contract 2019-02496. DanMAX is funded by the NUFI grant no. 4059-00009B. We thank the Danish Agency for Science, Technology, and Innovation for funding the instrument centre DanScatt. This work was also supported by the Danish Ministry for Higher Education and Science through the SMART Lighthouse. This project has received funding from the European Union's Horizon 2020 research and innovation programme under grant agreement No 957189. The project is part of BATTERY 2030+, the large-scale European research initiative for inventing the sustainable batteries of the future.

Appendix A. Supplementary data

Supplementary material related to this article can be found online at https://doi.org/10.1016/j.jpowsour.2023.232993.

References

[1] Hannah Ritchie, Cars, planes, trains: where do CO2 emissions from transport come from?, Tech report, Our World in Data, 2020.

[2] Ming Jiang, Dmitri L. Danilov, Rüdiger-A. Eichel, Peter H.L. Notten, A review of degradation mechanisms and recent achievements for Ni-rich cathode-based Li-ion batteries, Adv. Energy Mater. 11 (48) (2021).

[3] P. Li, H. Kim, S.-T. Myung, Y.-K. Sun, Diverting exploration of silicon anode into practical way: A review focused on silicon-graphite composite for lithium ion batteries, Energy Storage Mater. 35 (2021) 550–576, https://linkinghub.elsevier.com/retrieve/pii/S2405829720304384.

[4] M. Wetjen, D. Pritzl, R. Jung, S. Solchenbach, R. Ghadimi, H.A. Gasteiger, Differentiating the degradation phenomena in silicon-graphite electrodes for lithium-ion batteries, J. Electrochem. Soc. 164 (12) (2017) A2840–A2852, https://iopscience.iop.org/article/10.1149/2.1921712jes.

[5] S. Chae, S.-H. Choi, N. Kim, J. Sung, J. Cho, Integration of graphite and silicon anodes for the commercialization of high-energy lithium-ion batteries, Angew. Chem. Int. Edn 59 (1) (2020) 110–135, _eprint: https://onlinelibrary.wiley.com/doi/pdf/10.1002/anie.201902085.

[6] Q. Shi, J. Zhou, S. Ullah, X. Yang, K. Tokarska, B. Trzebicka, H.Q. Ta, M.H. Rümmeli, A review of recent developments in Si/C composite materials for Li-ion batteries, Energy Storage Mater. 34 (2021) 735–754, https://linkinghub.elsevier.com/retrieve/pii/S2405829720304037.

[7] X. Su, Q. Wu, J. Li, X. Xiao, A. Lott, W. Lu, B.B. Sheldon, J. Wu, Silicon-based nanomaterials for lithium-ion batteries: A review, Adv. Energy Mater. 4 (1) (2014) 1300882, _eprint: https://onlinelibrary.wiley.com/doi/pdf/10.1002/aenm.201300882.

[8] C. Heubner, T. Liebmann, O. Lohrberg, S. Cangaz, S. Maletti, A. Michaelis, Understanding component-specific contributions and internal dynamicsin silicon/graphite blended electrodes for high-energy lithium-ion batteries, Batter. Supercaps 5 (1) (2022) e202100182, _eprint: https://onlinelibrary.wiley.com/doi/pdf/10.1002/batt.202100182.

[9] X.H. Liu, H. Zheng, L. Zhong, S. Huang, K. Karki, L.Q. Zhang, Y. Liu, A. Kushima, W.T. Liang, J.W. Wang, J.-H. Cho, E. Epstein, S.A. Dayeh, S.T. Picraux, T. Zhu, J. Li, J.P. Sullivan, J. Cumings, C. Wang, S.X. Mao, Z.Z. Ye, S. Zhang, J.Y. Huang, Anisotropic swelling and fracture of silicon nanowires during lithiation, Nano Lett. 11 (8) (2011) 3312–3318, https://pubs.acs.org/doi/10.1021/nl201684d.

[10] X.H. Liu, L. Zhong, S. Huang, S.X. Mao, T. Zhu, J.Y. Huang, Size-dependent fracture of silicon nanoparticles during lithiation, ACS Nano 6 (2) (2012) 1522–1531, https://pubs.acs.org/doi/10.1021/nn204476h.

[11] C. Liu, O. Arcelus, T. Lombardo, H. Oularbi, A.A. Franco, Towards a 3D-resolved model of Si/Graphite composite electrodes from manufacturing simulations, J. Power Sources 512 (2021) 230486, https://linkinghub.elsevier.com/retrieve/pii/S0378775321009897.

[12] J. Bareño, I.A. Shkrob, J.A. Gilbert, M. Klett, D.P. Abraham, Capacity fade and its mitigation in Li-ion cells with silicon-graphite electrodes, J. Phys. Chem. C 121 (38) (2017) 20640–20649, https://pubs.acs.org/doi/10.1021/acs.jpcc.7b06118.

[13] H. Liu, A.J. Naylor, A.S. Menon, W.R. Brant, K. Edström, R. Younesi, Understanding the roles of tris(trimethylsilyl) phosphite (TMSPi) in LiNi0.8Mn0.1Co0.1O2 (NMC811)/silicon–graphite (Si–Gr) lithium-ion batteries, Adv. Mater. Interfaces 7 (15) (2020) 2000277, _eprint: https://onlinelibrary.wiley.com/doi/pdf/10.1002/admi.202000277.

[14] P. Pietsch, D. Westhoff, J. Feinauer, J. Eller, F. Marone, M. Stampanoni, V. Schmidt, V. Wood, Quantifying microstructural dynamics and electrochemical activity of graphite and silicon-graphite lithium ion battery anodes, Nature Commun. 7 (1) (2016) 12909, http://www.nature.com/articles/ncomms12909.

[15] G.E. Blomgren, The development and future of lithium ion batteries, J. Electrochem. Soc. 164 (1) (2017) A5019–A5025, https://iopscience.iop.org/article/10.1149/2.0251701jes.

[16] R. Schmuch, R. Wagner, G. Hörpel, T. Placke, M. Winter, Performance and cost of materials for lithium-based rechargeable automotive batteries, Nat. Energy 3 (4) (2018) 267–278, http://www.nature.com/articles/s41560-018-0107-2.

[17] F. Jeschull, Y. Surace, S. Zürcher, G. Lari, M.E. Spahr, P. Novák, S. Trabesinger, Graphite particle-size induced morphological and performance changes of graphite–silicon electrodes, J. Electrochem. Soc. 167 (10) (2020) 100535, https://iopscience.iop.org/article/10.1149/1945-7111/ab9b9a.

[18] J. Moon, H.C. Lee, H. Jung, S. Wakita, S. Cho, J. Yoon, J. Lee, A. Ueda, B. Choi, S. Lee, K. Ito, Y. Kubo, A.C. Lim, J.G. Seo, J. Yoo, S. Lee, Y. Ham, W. Baek, Y.-G. Ryu, I.T. Han, Interplay between electrochemical reactions and mechanical responses in silicon–graphite anodes and its impact on degradation, Nature Commun. 12 (1) (2021) 2714, http://www.nature.com/articles/s41467-021-22662-7.

[19] E. Moyassari, T. Roth, S. Kücher, C.-C. Chang, S.-C. Hou, F.B. Spingler, A. Jossen, The role of silicon in silicon-graphite composite electrodes regarding specific capacity, cycle stability, and expansion, J. Electrochem. Soc. 169 (1) (2022) 010504, https://iopscience.iop.org/article/10.1149/1945-7111/ac4545.

[20] J.-M. Lim, T. Hwang, D. Kim, M.-S. Park, K. Cho, M. Cho, Intrinsic origins of crack generation in Ni-rich LiNi0.8Co0.1Mn0.1O2 layered oxide cathode material, Sci. Rep. 7 (1) (2017) 39669, http://www.nature.com/articles/srep39669.

[21] D. Vidal, C. Leys, B. Mathieu, N. Guillet, V. Vidal, D. Borschneck, P. Chaurand, S. Genies, E. De Vito, M. Tulodziecki, W. Porcher, Si–C/G based anode swelling and porosity evolution in 18650 casing and in pouch cell, J. Power Sources 514 (2021) 230552, https://linkinghub.elsevier.com/retrieve/pii/S0378775321010508.

[22] K. Richter, T. Waldmann, N. Paul, N. Jobst, R.-G. Scurtu, M. Hofmann, R. Gilles, M. Wohlfahrt-Mehrens, Low-temperature charging and aging mechanisms of Si/C composite anodes in Li-ion batteries: An operando neutron scattering study, ChemSusChem 13 (3) (2020) 529–538, _eprint: https://onlinelibrary.wiley.com/doi/pdf/10.1002/cssc.201903139.

[23] L. Cai, K. An, Z. Feng, C. Liang, S.J. Harris, In-situ observation of inhomogeneous degradation in large format Li-ion cells by neutron diffraction, J. Power Sources 236 (2013) 163–168, https://linkinghub.elsevier.com/retrieve/pii/S0378775313003510.

[24] V. Baran, M.J. Mühlbauer, M. Schulz, J. Pfanzelt, A. Senyshyn, In operando studies of rotating prismatic Li-ion batteries using monochromatic wide-angle neutron diffraction, J. Energy Storage 24 (2019) 100772, https://linkinghub.elsevier.com/retrieve/pii/S2352152X19300623.

[25] G.S. Mattei, Z. Li, A.A. Corrao, C. Niu, Y. Zhang, B. Liaw, C.C. Dickerson, J. Xiao, E.J. Dufek, P.G. Khalifah, High-energy lateral mapping (HELM) studies of inhomogeneity and failure mechanisms in NMC622/Li pouch cells, Chem. Mater. 33 (7) (2021) 2378–2386, https://pubs.acs.org/doi/10.1021/acs.chemmater.0c04537.

[26] M. Mühlbauer, A. Schökel, M. Etter, V. Baran, A. Senyshyn, Probing chemical heterogeneity of Li-ion batteries by in operando high energy X-ray diffraction radiography, J. Power Sources 403 (2018) 49–55, https://linkinghub.elsevier.com/retrieve/pii/S0378775318310061.

[27] D. Petz, M. Mühlbauer, V. Baran, M. Frost, A. Schökel, C. Paulmann, Y. Chen, D. Garcés, A. Senyshyn, Lithium heterogeneities in cylinder-type Li-ion batteries – fatigue induced by cycling, J. Power Sources 448 (2020) 227466, https://linkinghub.elsevier.com/retrieve/pii/S0378775319314594.

[28] M. Mühlbauer, D. Petz, V. Baran, O. Dolotko, M. Hofmann, R. Kostecki, A. Senyshyn, Inhomogeneous distribution of lithium and electrolyte in aged Li-ion cylindrical cells, J. Power Sources 475 (2020) 228690, https://linkinghub.elsevier.com/retrieve/pii/S0378775320309940.

[29] H. Charalambous, D.P. Abraham, A.R. Dunlop, S.E. Trask, A.N. Jansen, T.R. Tanim, P.R. Chinnam, A.M. Colclasure, W. Xu, A.A. Yakovenko, O.J. Borkiewicz, L.C. Gallington, U. Ruett, K.M. Wiaderek, Y. Ren, Revealing causes of macroscale heterogeneity in lithium ion pouch cells via synchrotron X-ray diffraction, J. Power Sources 507 (2021) 230253, https://linkinghub.elsevier.com/retrieve/pii/S0378775321007722.

[30] K.V. Graae, P. Norby, Time- and space-resolved in situ X-ray diffraction study of phase transformations and redistribution in Zn–air battery anodes, ACS Applied Energy Materials 5 (9) (2022) 11392–11401, https://pubs.acs.org/doi/10.1021/acsaem.2c01868.

[31] M.K. Christensen, J.K. Mathiesen, S.B. Simonsen, P. Norby, Transformation and migration in secondary zinc–air batteries studied by *in situ* synchrotron X-ray diffraction and X-ray tomography, J. Mater. Chem. A 7 (11) (2019) 6459–6466, http://xlink.rsc.org/?DOI=C8TA11554K.

[32] P. Fischer, G. Frey, M. Koch, M. Ko, R. Thut, N. Schlumpf, R. Bu, High-resolution powder di!ractometer HRPT for thermal neutrons at SINQ, Physica B 276-278 (2000) 146–147.

[33] A.A. Coelho, TOPAS and TOPAS-Academic: an optimization program integrating computer algebra and crystallographic objects written in C++, J. Appl. Crystallogr. 51 (2018) 210–218.

[34] M.R. Rowles, C.E. Buckley, Aberration corrections for non-Bragg–Brentano diffraction geometries, J. Appl. Crystallogr. 50 (1) (2017) 240–251, https://scripts.iucr.org/cgi-bin/paper?S1600576717000085.

[35] K. Märker, P.J. Reeves, C. Xu, K.J. Griffith, C.P. Grey, Evolution of structure and lithium dynamics in $LiNi_{0.8}Mn_{0.1}Co_{0.1}$ O_2 (NMC811) cathodes during electrochemical cycling, Chem. Mater. 31 (7) (2019) 2545–2554, https://pubs.acs.org/doi/10.1021/acs.chemmater.9b00140.

[36] A. Senyshyn, O. Dolotko, M.J. Mühlbauer, K. Nikolowski, H. Fuess, H. Ehrenberg, Lithium intercalation into graphitic carbons revisited: Experimental evidence for twisted bilayer behavior, J. Electrochem. Soc. 160 (5) (2013) A3198–A3205, https://iopscience.iop.org/article/10.1149/2.031305jes.

[37] B. Hinrichsen, R.E. Dinnebier, M. Jansen, Two-dimensional diffraaction using area detectors, in: Powder Diffraction Theory and Practice, RSC Publishing, 2008, pp. 414–437.

[38] D.L. Bish, J.E. Post (Eds.), Modern Powder Diffraction, De Gruyter, Berlin, Boston, 2018.

[39] H. Khan, A. Yerramilli, A. D'Oliveira, T.L. Alford, D.C. Boffito, G.S. Patience, Experimental methods in chemical engineering: X-ray diffraction spectroscopy—XRD, Can. J. Chem. Eng. (98) (2020) 1255–1266.

[40] C.L. Berhaut, D.Z. Dominguez, P. Kumar, P.-H. Jouneau, W. Porcher, D. Aradilla, S. Tardif, S. Pouget, S. Lyonnard, Multiscale multiphase lithiation and delithiation mechanisms in a composite electrode unraveled by simultaneous *operando* small-angle and wide-angle X-Ray Scattering, ACS Nano 13 (10) (2019) 11538–11551, https://pubs.acs.org/doi/10.1021/acsnano.9b05055.